AIAA JOURNAL
Vol. 46, No. 4, April 2008

Advanced Analysis on Tiltrotor Aircraft Flutter Stability, Including Unsteady Aerodynamics

Taeseong Kim* and SangJoon Shin†
Seoul National University, Seoul 151-744, Republic of Korea

DOI: 10.2514/1.33474

The whirl-flutter-instability phenomenon imposes a serious limit on the forward speed in tiltrotor aircraft. In this paper, an advanced analysis is formulated to predict an aeroelastic stability for a gimballed three-bladed rotor with flexible wing based on three different types of aerodynamic model. Among them, the one with the full unsteady aerodynamics is most sophisticated, because it may represent more realistic operating conditions. A nine-degree-of-freedom model is newly developed to predict the complete tiltrotor aircraft. Numerical results are obtained in both time and frequency domains. A generalized eigenvalue is used to estimate whirl-flutter stability in the frequency domain, and the Runge–Kutta method is used in the time domain. Control system flexibility is further included in the present analysis to give the capability for a more accurate stability prediction. Results from such an improved analysis are validated with the other existing predictions and show good agreement. The present model with unsteady aerodynamics will be extended to further consider an aerodynamic interaction between the rotor and wing.

Nomenclature

a	=	rotor blade section two-dimensional lift-curve slope
a_h	=	distance from the pivot point to the aerodynamic center
b	=	half-chord of airfoil
C	=	damping matrix
C_H	=	rotor vertical force coefficient
$C(k)$	=	lift-deficiency function
C_{Mx}	=	rotor lateral moment coefficient
C_{My}	=	rotor longitudinal moment coefficient
C_T	=	rotor thrust coefficient
C_Y	=	rotor side force coefficient
c	=	rotor blade chord
D	=	blade section drag force per unit length
F_r	=	blade section radial aerodynamic force per unit length
F_x	=	blade section in-plane aerodynamic force per unit length
F_z	=	blade section out-of-plane aerodynamic force per unit length
G_a	=	pitch input coefficient matrix
H	=	rotor H-force
h_m	=	rotor mast height
$\dot{h}$	=	velocity of the flapping motion
I_b	=	characteristic inertia of blade flapping
I_p	=	rotor blade pitch moment of inertia
I_x	=	pylon yaw moment of inertia
I_y	=	pylon pitch moment of inertia
I_β	=	blade flap inertia
I_ζ	=	blade lag inertia
K	=	blade stiffness matrix
K_x	=	pylon yaw spring constant
K_y	=	pylon pitch spring constant
K_P	=	rotor blade pitch-flap coupling
$K_{P\zeta}$	=	rotor blade pitch-lag coupling
L	=	blade section lift force per unit length
L_C	=	circulatory part of blade section lift force
L_{NC}	=	noncirculatory part of blade section lift force
M	=	blade mass matrix
M_x	=	rotor lateral hub moment
M_y	=	rotor longitudinal hub moment
M_β	=	net flap moment
m_p	=	pylon mass
N	=	number of blade
p	=	wing torsion mode
Q	=	downwash velocity at three-quarter chord
q_1	=	wing vertical bending mode
q_2	=	wing chordwise bending mode
R	=	rotor blade radius
S_β	=	first moment of inertia in flap mode
S_ζ	=	first moment of inertia in lag mode
s	=	Laplace variable in transfer function
T	=	rotor thrust
U	=	blade section resultant velocity
U_P	=	blade section out-of-plane velocity
U_R	=	blade section radial velocity
U_T	=	blade section in-plane velocity
u_G	=	longitudinal aerodynamic gust velocity
V	=	aircraft forward velocity
v	=	rotor-induced inflow
X_1, X_2	=	augmented state variables
x	=	vertical axis
Y	=	rotor side force
y	=	lateral axis
y_p	=	rotor shaft vertical displacement
y_{Tw}	=	cantilever wing length
Z_a	=	gust coefficient matrix
z	=	longitudinal axis
z_P	=	rotor shaft longitudinal displacement
α_G	=	vertical aerodynamic gust velocity
α_x	=	rotor shaft yaw angle at pivot
α_y	=	rotor shaft pitch angle at pivot
α_z	=	rotor shaft roll angle at pivot
β	=	blade flapping angle
β_G	=	lateral aerodynamic gust velocity
β_{1C}	=	rotor longitudinal flapping degree of freedom
β_{1S}	=	rotor lateral flapping degree of freedom
γ	=	Lock number
$\Delta()\delta()$	=	small variation in a quantity
δu_P	=	component of perturbation in u_P

Received 15 July 2007; revision received 14 November 2007; accepted for publication 30 November 2007.

*Research Assistant, School of Mechanical and Aerospace Engineering, Building 301, Room 1313, Shillim-Dong, Kwanak-Gu; kimts77@snu.ac.kr.

†Assistant Professor, Institute of Advanced Aerospace Technology, School of Mechanical and Aerospace Engineering, Building 301, Room 1418, Shillim-Dong, Kwanak-Gu; ssjoon@snu.ac.kr. Member AIAA.

δu_T = component of perturbation in u_T
δ_3 = rotor blade pitch/flap coupling
ζ = blade lag angle
ζ_{1C} = rotor cyclic lag degree of freedom
ζ_{1S} = rotor cyclic lag degree of freedom
θ = blade pitch angle
θ_0 = rotor collective pitch control input
ρ = air density
σ = rotor solidity
υ_β = rotating blade flapping natural frequency
υ_ζ = rotating blade lag natural frequency
Φ = blade inflow angle
Ψ = rotor blade azimuth angle
Ω = rotor rotational speed
ω_θ = natural frequency corresponding to the rotor blade rigid-pitch motion
$()_0$ = trim quantity
$\bar{()}$ = $d/d\Psi$
$\underline{\ }$ = dimensionless quantity

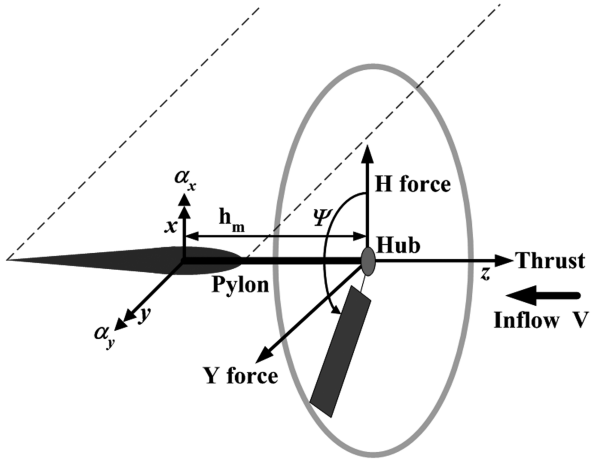

Fig. 1 Totally rigid-bladed rotor system.

I. Introduction

THE whirl-flutter instability, which is induced by an in-plane hub force in a rotor, generally governs the maximum cruise speed in a tiltrotor aircraft. Precise estimation of the whirl-flutter instability is thus required to improve the cruise performance. Hall [1] analyzed a few principal destabilizing factors for rotor/pylon whirl flutter, and further research was conducted to improve whirl-flutter stability. Johnson [2] performed a rigid-blade analysis and validated it with the experimental data. He extended the analysis to use the coupled blade bending and torsion modes and the nonaxial flow, which enabled an analysis of the helicopter mode and the conversion operation [3,4]. Higher-harmonic control was experimentally employed at both the rotor swashplate and the wing flaperon to reduce vibrations in airplane mode [5]. In [6], generalized predictive control was experimentally investigated to evaluate the effectiveness of an adaptive control algorithm. More recently, a refined active-control algorithm employed via actuation of the wing flaperon and the rotor swashplate was examined for whirl-flutter stability and robustness augmentation [7].

It is observed that the previous analytical investigations have not considered an unsteady aerodynamic environment. Many researchers indicated that unsteady aerodynamic effects may not be significant to the whirl-flutter stability in tiltrotor aircraft. However, there have not been any analytical results in the literature regarding quantitative estimation of unsteady aerodynamics, which may affect the whirl-flutter stability in tiltrotor aircraft.

This paper provides a description of an advanced analytical model with three different aerodynamic models. It is difficult to predict an influence of unsteady aerodynamic effects upon the whirl-flutter stability, because unsteady aerodynamics is believed to play a certain part in whirl-flutter stability and thus airframe vibration. In this paper, a nine-degree-of-freedom (9-DOF) model is developed to predict and enhance the whirl-flutter stability, including an unsteady aerodynamic model. A less detailed 4-DOF model is previously established by the authors and is explained in [8]. The present 9-DOF model is more complete than the previous 4-DOF model, because a lead-lag motion of the rotor blade and a flexible-wing motion are newly included.

II. Analytical Model

To analyze an aeroelastic characteristic of a tiltrotor aircraft, relevant formulation is divided into three parts (i.e., rotor, wing, and shaft). For the present modeling of a rotor, the flap, lag, and shaft motions are considered in the structural formulation and three different types of aerodynamic models are used in the aerodynamic formulation: two quasi-steady models and one full unsteady aerodynamic model. For an elastic wing, vertical q_1 and lateral q_2 bending and torsion p are considered in the structural part with the similar aerodynamic models. The motion of the rotor shaft needs to be expressed in terms of the wing degrees of freedom. The shaft displacements x_P, y_P, and z_P and rotations α_x, α_y, and α_z at a pivot point are transmitted to the wing degrees of freedom, because the rotor motion is directly transmitted to the wing through the shaft. More detailed explanations are presented in the following sections.

A. Rotor Equations of Motion

1. Structural Modeling

The structural part of the rotor system, which is presented in Fig. 1, is based on a typical helicopter configuration; however, a few modifications are needed because of several additional degrees of freedom. The present model then consists of 12 degrees of freedom: three each for blade flapping (β_0, β_{1C}, and β_{1S}) and lead-lag (ς_0, ς_{1C}, and ς_{1S}) motions in the rotor and three each for translation (x_p, y_p, and z_p) and rotational (α_x, α_y, and α_z) motions of the rotor shaft. When it is combined with the full unsteady aerodynamic model, four degrees of freedom will be added, which are augmented state variables X_{1C}, X_{1S}, X_{2C}, and X_{2S}. They are explained in detail in the following Aerodynamic Modeling section.

A flapping and lead-lag degree of freedom is used to describe a motion of the completely rigid gimballed three-bladed rotor system assumed in the present paper. Considering force and moment equilibrium, the following equations are obtained, which represent the rotor and shaft motion:

$$I_\beta(\ddot{\beta}_m + \nu_\beta^2\beta_m + I_{\beta\alpha}[-(\ddot{\alpha}_y - 2\Omega\dot{\alpha}_x)\cos\psi_m + (\ddot{\alpha}_x + 2\Omega\dot{\alpha}_y)\sin\psi_m] + S_\beta\ddot{z}_P) = M_{F_m} \quad (1)$$

$$I_\varsigma(\ddot{\varsigma}_m + \nu_\varsigma^2\varsigma_m + S_\varsigma[(\ddot{x}_P + h_m\ddot{\alpha}_y)\sin\psi_m - (\ddot{y}_P - h_m\ddot{\alpha}_x)\cos\psi_m] - I_{\varsigma\alpha}\ddot{\alpha}_z) = M_{L_m} \quad (2)$$

Equations (1) and (2) are, respectively, moment equilibrium equations of flap and lag in a rotating frame. Employing the Fourier coordinate transformation, it is possible to convert these equations into those in a nonrotating frame. The equations are also nondimensionalized with respect to ρ, Ω, R, I_b, γ, σ, and $I_b(N/2)$. The structural part of the rotor equations of motion is arranged on the left-hand side (LHS) in the preceding equations and the aerodynamic part is on the right-hand side (RHS).

2. Aerodynamic Modeling

The aerodynamic formulations are obtained with an assumption that the tiltrotor aircraft is in a purely axial flow in equilibrium. Only a perturbation component in aerodynamics is considered in this paper. The trim state is assumed to be established already and the perturbation from it is only considered for an aeroelastic stability analysis.

The rotor aerodynamic forces and moments are presented in the RHS of Eqs. (1) and (2). Three different kinds of aerodynamic model are developed in the present paper, both in time and frequency domains: two quasi-steady models and one unsteady aerodynamic model. The first aerodynamic model is widely used and is referred to as a normal quasi-steady aerodynamics in this paper. This aerodynamic model is developed based on [2] and is described in Eq. (3). The second quasi-steady aerodynamic model is presented in Eq. (4). It is equivalent to replacing $C(k)$ with 1 in Greenberg's aerodynamic model [9–11]. This model is cited as Greenberg's quasi-steady aerodynamics through the present paper. For a full unsteady aerodynamic representation, Greenberg's two-dimensional unsteady aerodynamic model is used [10–13]. Its expression is presented in Eq. (5). In Eqs. (4) and (5), noncirculatory terms are ignored, because a thin airfoil theory is adapted in the present derivation, and thus the effects of noncirculatory terms are believed to be very small compared with the circulatory terms [14]. In the present paper, a generalized Greenberg's aerodynamic formulation, which is modified for a rotary-wing aircraft by Friedmann and Yuan [12], is used to derive the quasi-steady and unsteady aerodynamic models, because such a simple aerodynamic model based on a strip theory requires relatively small computational effort to obtain a reasonable result. The present formulation is also useful for a finite time arbitrary motion in a coupled flap–lag–torsion aeroelastic analysis of a rotating blade [11,15]. The foregoing development of the state-space form is also suitable with the present formulation of Greenberg's unsteady aerodynamics [11,13]:

$$L = 2\pi\rho U(t)^2 b\alpha(t) \tag{3}$$

$$L = \underbrace{2\pi\rho U(t)b\left[(\dot{h}(t) + U(t)\theta(t)) + b\left(\frac{1}{2} - a_h\right)\dot{\theta}(t)_{\text{ref}}\right]}_{\text{circulatory part}(L_C)} + \underbrace{\pi\rho b^2[(\dot{h}(t) + U(t)\theta(t))\dot{} - ba_h\ddot{\theta}(t)_{\text{ref}}]}_{\text{noncirculatory part}(L_{\text{NC}})} \tag{4}$$

$$L = \underbrace{2\pi\rho U(t)bC(k)\left[(\dot{h}(t) + U(t)\theta(t)) + b\left(\frac{1}{2} - a_h\right)\dot{\theta}(t)_{\text{ref}}\right]}_{\text{circulatory part}(L_C)} + \underbrace{\pi\rho b^2[(\dot{h}(t) + U(t)\theta(t))\dot{} - ba_h\ddot{\theta}(t)_{\text{ref}}]}_{\text{noncirculatory part}(L_{\text{NC}})} \tag{5}$$

The aerodynamic environment of a typical rotor blade section is presented in Fig. 2. All the velocities and forces are estimated with respect to the reference frame, which is a hub plane. The aerodynamic forces acting on a blade typical section are lift L and drag D. The total forces in the x and z directions can be obtained as follows:

$$\frac{\bar{F}_z}{a\bar{c}} = \frac{\bar{L}}{a\bar{c}}\cos\phi - \frac{\bar{D}}{a\bar{c}}\sin\phi \tag{6}$$

$$\frac{\bar{F}_x}{a\bar{c}} = \frac{\bar{L}}{a\bar{c}}\sin\phi + \frac{\bar{D}}{a\bar{c}}\cos\phi \tag{7}$$

where $\sin\phi = [u_p(\psi)]/[U(\psi)]$, and $\bar{L}$ and $\bar{D}$ are the nondimensionalized terms, which are divided by $\rho\Omega^2R^3$.

The aerodynamic forces acting on a blade are dominated by the lift in a rotor flowfield with a high inflow. Thus, the drag forces are not included and only $C_{l\alpha}$ terms are retained. Then Eqs. (6) and (7) can be simplified as follows:

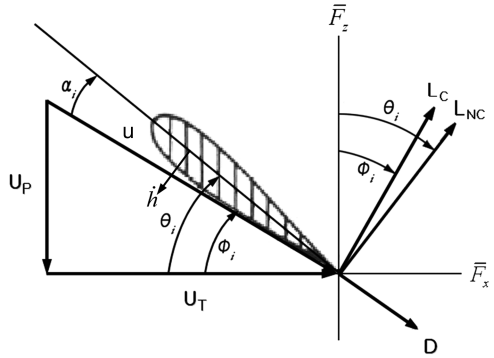

Fig. 2 Resultant and inflow velocity on a typical blade section.

$$\frac{\bar{F}_z}{a\bar{c}} = \frac{\bar{L}}{a\bar{c}}\frac{u_T(\psi)}{U(\psi)} \tag{8}$$

$$\frac{\bar{F}_x}{a\bar{c}} = \frac{\bar{L}}{a\bar{c}}\frac{u_P(\psi)}{U(\psi)} \tag{9}$$

$$\frac{\bar{F}_r}{a\bar{c}} = \bar{U}\bar{u}_R\frac{C_d}{2a} - \beta\frac{\bar{F}_z}{a\bar{c}} \simeq -\beta\frac{\bar{F}_z}{a\bar{c}} \tag{10}$$

According to the assumption used in the present paper, which is that only perturbation terms in aerodynamics are to be considered, Eqs. (3–5) can be divided into two terms (trim and perturbation) and simplified as follows:

$$L = 2\pi\rho b\{U_0 + \delta U(t)\}^2\{\alpha_0 + \delta\alpha(t)\} \tag{11}$$

$$L = 2\pi\rho bU(t)\Big[-\delta u_p(t)\cos\phi + \delta u_T(t)\sin\phi + U(t)\theta(t) + b(\tfrac{1}{2} - a_h)\delta\dot{\theta}_{\text{ref}}\Big] = 2\pi\rho bU(t)Q(t) = 2\pi\rho b\{U_0 + \delta U(t)\}Q(t) \tag{12}$$

$$L = 2\pi\rho bU(t)C(k)\Big[-\delta u_p(t)\cos\phi + \delta u_T(t)\sin\phi + U(t)\theta(t) + b(\tfrac{1}{2} - a_h)\delta\dot{\theta}_{\text{ref}}\Big] = 2\pi\rho bU(t)C(k)Q(t) = 2\pi\rho b\{U_0 + \delta U(t)\}C(k)Q(t) \tag{13}$$

where

$$Q(t) = [-\delta u_p(t)\cos\phi + \delta u_T(t)\sin\phi + U(t)\theta(t) + b(\tfrac{1}{2} - a_h)\delta\dot{\theta}_{\text{ref}}]$$

$\theta(t) = \alpha_0 + \delta\theta$, $\delta\theta = -\beta K_P$, $u_T(t) = u_{T_0} + \delta u_T(t)$, $u_P(t) = u_{P_0} + \delta u_P(t)$, and $\dot{h} = -\delta u_p(t)\cos\phi + \delta u_T(t)\sin\phi$.

The detailed expressions of the perturbation velocity terms are presented in Appendix A.

The preceding expressions can be used for the two quasi-steady aerodynamic models. However, for the full unsteady aerodynamic model, expressions of the forces and moments are slightly different because of the lift-deficiency function $C(k)$. This function is represented only in the frequency domain, as in Eq. (5). Therefore, Jones's approximation, which is shown next, is used to express the lift-deficiency function in the time domain [16,17].

$$C(k) = \left[\frac{0.5\bar{s}^2 + 0.2808\bar{s} + 0.01365}{\bar{s}^2 + 0.3455\bar{s} + 0.01365}\right] \tag{14}$$

where $\bar{s} = s(\bar{b}R/U_0)$.

By substituting Eq. (14) into Eq. (5), a state-space equation is obtained as follows:

$$\begin{Bmatrix}\dot{X}_1\\ \dot{X}_2\end{Bmatrix} = \begin{bmatrix}a_{11} & a_{12}\\ 1 & 0\end{bmatrix}\begin{Bmatrix}X_1\\ X_2\end{Bmatrix} + \begin{Bmatrix}1\\ 0\end{Bmatrix}Q(t)$$
$$y = [C \;\; D]\begin{Bmatrix}X_1\\ X_2\end{Bmatrix} + 0.5Q(t) \tag{15}$$

where $a_{11} = -0.3455(U_0/\bar{b}R)$, $a_{12} = -0.0137(U_0/\bar{b}R)^2$, $C = 0.1081(U_0/\bar{b}R)$, and $D = 0.0068(U_0/\bar{b}R)^2$.

From Eq. (15), new state-space equations for the augmented state variables and circulatory part of the lift can be formulated as a dimensionless form:

$$\begin{Bmatrix}\dot{\bar{X}}_1\\ \dot{\bar{X}}_2\end{Bmatrix} = \begin{bmatrix}a_{11} & a_{12}\\ 1 & 0\end{bmatrix}\begin{Bmatrix}\bar{X}_1\\ \bar{X}_2\end{Bmatrix} + \begin{Bmatrix}1\\ 0\end{Bmatrix}Q(\psi)$$
$$\bar{L}_c = 2\pi b U(\psi)\{C\bar{X}_1 + D\bar{X}_2 + 0.5Q(\psi)\} \tag{16}$$

where $X_1 = R\bar{X}_1$, $X_2 = (R/\Omega)\bar{X}_2$, and $(\partial/\partial t) = \Omega(\partial/\partial\psi)$.

In Eq. (16), the augmented state variables $\bar{X}_1$ and $\bar{X}_2$ are associated with a downwash velocity at the three-quarter-chord location [15]. They are used to describe the unsteady effect. These augmented states are driven by the time history of $Q(\psi)$ at each spanwise location. However, in this paper, those corresponding to the three-quarter-span location are used for a representative averaged value. A Fourier coordinate transformation may be applied to express $Q(\psi)$, $\bar{X}_1$, and $\bar{X}_2$ in a nonrotating system:

$$Q(\psi) = \bar{Q}_0 + \sum_{n=1}^{\mathrm{NH}} \bar{Q}_{1cn}\cos n\psi + \bar{Q}_{1sn}\sin n\psi$$
$$\bar{X}_1 = \bar{X}_{1_0} + \sum_{n=1}^{\mathrm{NH}} \bar{X}_{1cn}\cos n\psi + \bar{X}_{1sn}\sin n\psi \tag{17}$$
$$\bar{X}_2 = \bar{X}_{2_0} + \sum_{n=1}^{\mathrm{NH}} \bar{X}_{2cn}\cos n\psi + \bar{X}_{2sn}\sin n\psi$$

where NH is the number of harmonics retained in the Fourier analysis.

By substituting Eq. (17) into Eq. (16), the lift expression is obtained for the full unsteady aerodynamic model for an analysis in the time domain.

In Fig. 3, the in-plane forces, which are H and Y in each blade, can be expressed as follows:

$$H_{\mathrm{force}} = F_x\sin\psi_m + F_r\cos\psi_m$$
$$Y_{\mathrm{force}} = -F_x\cos\psi_m + F_r\sin\psi_m \tag{18}$$

The net rotor aerodynamic forces and moments are obtained by integrating the section forces and moments over the span of the blade and summing over all three blades:

$$\frac{C_T}{\sigma a} = \frac{1}{N}\sum_m \int_0^1 \frac{\bar{F}_z}{a\bar{c}}\,\mathrm{d}\bar{r}$$
$$\frac{2C_H}{\sigma a} = \frac{2}{N}\sum_m\left(\cos\psi_m\int_0^1\frac{\bar{F}_r}{a\bar{c}}\,\mathrm{d}\bar{r} + \sin\psi_m\int_0^1\frac{\bar{F}_x}{a\bar{c}}\,\mathrm{d}\bar{r}\right)$$
$$\frac{2C_Y}{\sigma a} = \frac{2}{N}\sum_m\left(\sin\psi_m\int_0^1\frac{\bar{F}_r}{a\bar{c}}\,\mathrm{d}\bar{r} - \cos\psi_m\int_0^1\frac{\bar{F}_x}{a\bar{c}}\,\mathrm{d}\bar{r}\right) \tag{19}$$
$$\frac{\bar{M}_F}{ac} = \int_0^1 \bar{r}\frac{\bar{F}_z}{a\bar{c}}\,\mathrm{d}\bar{r}$$

The hub moment due to the rotor may be expressed in terms of the tip-path-plane tilt β_{1C} and β_{1S} as follows:

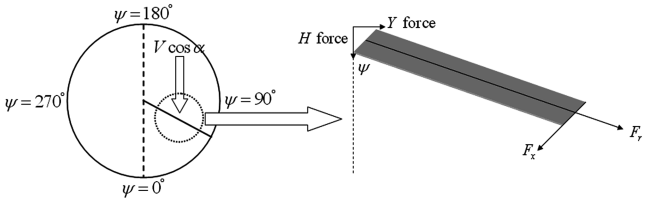

Fig. 3 *H* and *Y* forces on the blade.

$$\frac{2C_{My}}{\sigma a} = -\frac{\nu_\beta^2 - 1}{\gamma}\beta_{1c} \tag{20}$$

$$\frac{2C_{Mx}}{\sigma a} = \frac{\nu_\beta^2 - 1}{\gamma}\beta_{1s} \tag{21}$$

B. Wing Equations of Motion

The structural model of the wing, shown in Fig. 1, is elastically cantilevered at the fixed support. The equations of motion for the wing degrees of freedom are presented next:

$$(I_{q_w} + m_p y_{T_w}^2)\ddot{q}_1 + C_{q_1}\dot{q}_1 + K_{q_q}q_1 + S_w\ddot{p} = (M_{q_1})_{\mathrm{aero}} + (M_{q_1})_{\mathrm{rotor}} \tag{22}$$

$$(I_{q_w} + I_{p_x}\eta_w'^2 + m_p y_{T_w}^2)\ddot{q}_2 + C_{q_2}\dot{q}_2 + K_{q_2}q_2 = (M_{q_2})_{\mathrm{aero}} + (M_{q_2})_{\mathrm{rotor}} \tag{23}$$

$$(I_{q_w} + I_{p_y})\ddot{p} + C_p\dot{p} + K_p p + S_w\ddot{q}_1 = (M_p)_{\mathrm{aero}} + (M_p)_{\mathrm{rotor}} \tag{24}$$

Equations (22–24) are, respectively, moment equilibrium equations of vertical q_1 and lateral q_2 bending and torsion p in the fixed frame. They are also nondimensionalized with respect to ρ, Ω, R, I_b, γ, σ, and $I_b(N/2)$; there, we have inertia, structural damping, and spring terms. Those terms are influenced by wing aerodynamic forces and rotor hub forces and moments acting on the wing tip. However, the wing aerodynamic forces are not included in the present derivation. The rotor aerodynamic forces and moments are explained in the previous section.

C. Connection Between Rotor and Wing

To connect the rotor and wing models, a shaft motion needs to be expressed, because the effects of the rotor motion are transferred through the shaft to the wing. The equations of motion of the shaft are presented as follows:

$$\begin{pmatrix}\alpha_x\\ \alpha_y\\ \alpha_z\end{pmatrix} = \begin{bmatrix}0 & -\eta_w' y_{T_w} & 0\\ 0 & 0 & 1\\ -\eta_w' y_{T_w} & 0 & 0\end{bmatrix}\begin{pmatrix}q_1\\ q_2\\ p\end{pmatrix} \tag{25}$$

$$\begin{pmatrix}x_P\\ y_P\\ z_P\end{pmatrix} = \begin{bmatrix}\eta_w y_{T_w} & 0 & 0\\ 0 & 0 & 0\\ 0 & -\eta_w y_{T_w} & 0\end{bmatrix}\begin{pmatrix}q_1\\ q_2\\ p\end{pmatrix} \tag{26}$$

The detailed expression of the shaft motion is also presented in [2]. The wing torsion deflection p is associated with the shaft pitch α_y. The wing vertical bending q_1 results in vertical displacement x_P of the shaft. It also produces a slope of the elastic axis at the tip, and thus such vertical bending results in a shaft roll motion α_z. The wing chordwise bending q_2 is associated with longitudinal displacement z_P of the shaft and also shaft yaw angle α_x. The wing bending motion also produces a coupling in the rotor motion.

III. Aeroelastic Stability Analysis

After the rotor, wing, and connection equations are formulated, they need to be assembled as a governing equation. The detailed expression of the governing equation is presented in Appendix B. The governing equations are obtained in terms of 9 and 13 degrees of freedom for different aerodynamic models, which are quasi-steady and full unsteady aerodynamics, respectively. First, the governing equations with quasi-steady aerodynamic models are given. The governing equations for the normal and Greenberg's quasi-steady aerodynamic models result in the same form.

A. Quasi-Steady Aerodynamic Models

Substituting the forces and moments of the rotor, which are given in Eqs. (3) and (4), into the RHS of Eqs. (1), (2), and (22–24) gives the following expression:

$$\text{RHS} = C_a\dot{y} + K_a y + G_a p + Z_a g \tag{27}$$

where

$$y^T = \{\beta_{1C} \;\; \beta_{1S} \;\; \varsigma_{1C} \;\; \varsigma_{1S} \;\; \beta_0 \;\; \varsigma_0 \;\; q_1 \;\; q_2 \;\; p\}$$

$p^T = \{\theta_{1C} \;\; \theta_{1S} \;\; \theta_0\}$, $g^T = \{u_G \;\; \beta_G \;\; \alpha_G\}$, and the subscript a means an aerodynamic part.

The governing equation can be rewritten as follows:

$$M_s\ddot{y} + C_s\dot{y} + K_s y = C_a\dot{y} + K_a y + G_a p + Z_a g \tag{28}$$

where the subscript s means a structural part and all elements of the matrices are dimensionless.

For simplicity, Eq. (28) can be rearranged as

$$\begin{aligned} M_s\ddot{y} &= -(C_s - C_a)\dot{y} - (K_s - K_a)y + G_a p + Z_a g \\ \therefore \ddot{y} &= -M_s^{-1}(C_s - C_a)\dot{y} - M_s^{-1}(K_s - K_a)y + M_s^{-1}G_a p + M_s^{-1}Z_a g \\ &= -(M_s^{-1}\bar{C})\dot{y} - (M_s^{-1}\bar{K})y + M_s^{-1}G_a p + M_s^{-1}Z_a g \\ &= -A\dot{y} - By + \bar{G}p + \bar{Z}g \end{aligned} \tag{29}$$

where $\bar{C} = (C_s - C_a)$, $\bar{K} = (K_s - K_a)$, $A = (M_s^{-1}\bar{C})$, $B = (M_s^{-1}\bar{K})$, $\bar{G} = (M_s^{-1}G_a)$, and $\bar{Z} = (M_s^{-1}Z_a)$.

Converting Eq. (29) into a state-space form gives

$$\dot{Y} = \underbrace{\begin{bmatrix} 0 & I \\ -B & -A \end{bmatrix}}_{18\times18} \underbrace{\begin{Bmatrix} y \\ \dot{y} \end{Bmatrix}}_{18\times1} + \underbrace{\begin{bmatrix} 0 & 0 \\ \bar{G} & \bar{Z} \end{bmatrix}}_{18\times6} \underbrace{\begin{Bmatrix} p \\ g \end{Bmatrix}}_{6\times1} \tag{30}$$

where $Y^T \equiv \{y \;\; \dot{y}\}$.

B. Full Unsteady Aerodynamic Model

Ordinary differential equations corresponding to the augmented state variables are added to the preceding governing equations. Substituting the aerodynamic forces and moment into the structural equations, a state-space equation is obtained as follows:

$$\dot{Y} = \underbrace{\begin{bmatrix} 0 & I \\ -B & -A \end{bmatrix}}_{18\times18} \underbrace{\begin{Bmatrix} y \\ \dot{y} \end{Bmatrix}}_{18\times1} + \underbrace{\begin{Bmatrix} 0 \\ C \end{Bmatrix}}_{18\times4} \underbrace{X}_{4\times1} + \underbrace{\begin{bmatrix} 0 & 0 \\ \bar{G} & \bar{Z} \end{bmatrix}}_{18\times6} \underbrace{\begin{Bmatrix} p \\ g \end{Bmatrix}}_{6\times1} \tag{31}$$

where $X^T = (\bar{X}_{1C} \;\; \bar{X}_{1S} \;\; \bar{X}_{2C} \;\; \bar{X}_{2S})$.

Here, the equations corresponding to the augmented state variables describe the unsteady effects due to downwash at the quarter-chord point. Using Eqs. (31) and (16), a governing equation, which enables analysis in both the time and frequency domains, is obtained in the following state-space form:

$$\begin{bmatrix} \dot{Y} \\ \dot{X} \end{bmatrix} = \underbrace{\begin{bmatrix} \overset{*}{T} & \overset{*}{S} \\ D & E \end{bmatrix}}_{22\times22} \underbrace{\begin{bmatrix} Y \\ X \end{bmatrix}}_{22\times1} + \underbrace{\begin{bmatrix} \overset{*}{O} \\ 0 \end{bmatrix}}_{22\times6} \underbrace{\begin{bmatrix} p \\ g \end{bmatrix}}_{6\times1} \tag{32}$$

where

$$T^* = \underbrace{\begin{bmatrix} 0 & I \\ -B & -A \end{bmatrix}}_{18\times18}, \quad S^* = \underbrace{\begin{Bmatrix} 0 \\ C \end{Bmatrix}}_{18\times4}, \quad O^* = \underbrace{\begin{bmatrix} 0 & 0 \\ \bar{G} & \bar{Z} \end{bmatrix}}_{18\times6}$$

$$E = \begin{bmatrix} a_{11} & a_{12} \\ 1 & 0 \end{bmatrix}, \quad D = \begin{Bmatrix} 1 \\ 0 \end{Bmatrix}, \quad v = \underbrace{\begin{Bmatrix} p \\ g \end{Bmatrix}}_{6\times1}$$

$A = (\bar{M}^{-1}\bar{C})$, $B = (\bar{M}^{-1}\bar{K})$, $C = (\bar{M}^{-1}Z_a)$, $\bar{M} = (M_s - M_a)$, $\bar{C} = (C_s - C_a)$, $\bar{K} = (K_s - K_a)$, $\bar{G} = (M_s^{-1}G_a)$, and $\bar{Z} = (M_s^{-1}Z_a)$.

IV. Numerical Results

Numerical investigation is conducted by estimating whirl-flutter stability boundary with the developed model. It is assumed that the aircraft has reached a trim state; therefore, only perturbations are considered to obtain the results regarding whirl-flutter stability.

The structural and aerodynamic quantities used for a numerical investigation are based on a typical full-scale tiltrotor aircraft. The numerical values of the structural parameters are based on those in [2]. They are $h_m = 0.261$, $\gamma = 3.83$, $\nu_\beta = 1.02$, $\Omega = 458$ rpm, and $b = 0.047$. The operating condition considered in this paper is autorotation. In a state of autorotation, no restraint is imposed on the rotor rotation about the hub. Therefore, no rotor torque is transmitted to the shaft, and no pylon roll motion is transmitted to the rotor. This will be automatically accomplished by the zero spring rate. Because the perturbations in control pitch input and gust are not considered in the present analysis, $\bar{G}$, $\bar{Z}$, and O^* matrices will be ignored in Eqs. (30) and (32). To investigate whirl-flutter stability, aircraft flight speed is arbitrarily increased and its stability is evaluated while keeping the same structural parameters.

A. Normal Quasi-Steady Aerodynamic Model

This section presents the results of the normal quasi-steady aerodynamic model in which the lift is expressed in Eq. (3). Figure 4 shows the predicted variation of the system eigenvalues in terms of the flight speed. Progressive and regressive modes of the rotor flapping and lead lag motion are denoted by $\beta \pm 1$ and $\varsigma \pm 1$, respectively. The low frequencies of rotor flapping and lead lag motion, which are $\beta - 1$ and $\varsigma - 1$, cross the vertical q_1 and chordwise q_2 bending modes of the wing and affect the damping of the wing modes. When the $\beta - 1$ frequency approaches the vertical and chordwise bending modes, the vertical and chordwise damping modes are rapidly decreased. Figure 4b shows the damping ratio. The vertical bending mode of the wing has a maximum damping (where $\varsigma - 1$ and q_1 mode frequencies cross each other) at which the peak of the q_1 mode occurs, because $\varsigma - 1$ mode damping is greater than the q_1 mode. If $\varsigma - 1$ mode damping is lower than that of q_1 mode, then a valley appears. According to the figure, the q_1 mode becomes unstable first among the modes considered. Furthermore, q_2 and p modes become consecutively unstable.

Figures 5 illustrates the results obtained in the time and frequency domains, respectively, while numerically increasing aircraft speed from 165 to 256 m/s to find a stability boundary. To increase the flight speed of a practical tiltrotor aircraft, collective pitch needs to be adjusted. However, in the present numerical examination, the aircraft speed is increased in an arbitrary fashion. Figure 5a shows the results of the wing modes in the time domain. It is shown that the system remains stable until $V = 238$ m/s. However, the aircraft becomes unstable when its flight speed is higher than 238 m/s. Figure 5b shows q_1 and q_2 mode results in the frequency domain at the same flight speed. When the poles of the vertical bending mode of the wing are located on an imaginary axis, the aircraft is on the verge of flutter instability. If they are located in the right half-plane, the system is unstable. Based on the present aerodynamic model, it is observed that stability boundary is approximately 238 m/s, which is considered to be a practical whirl-flutter boundary for the present tiltrotor aircraft.

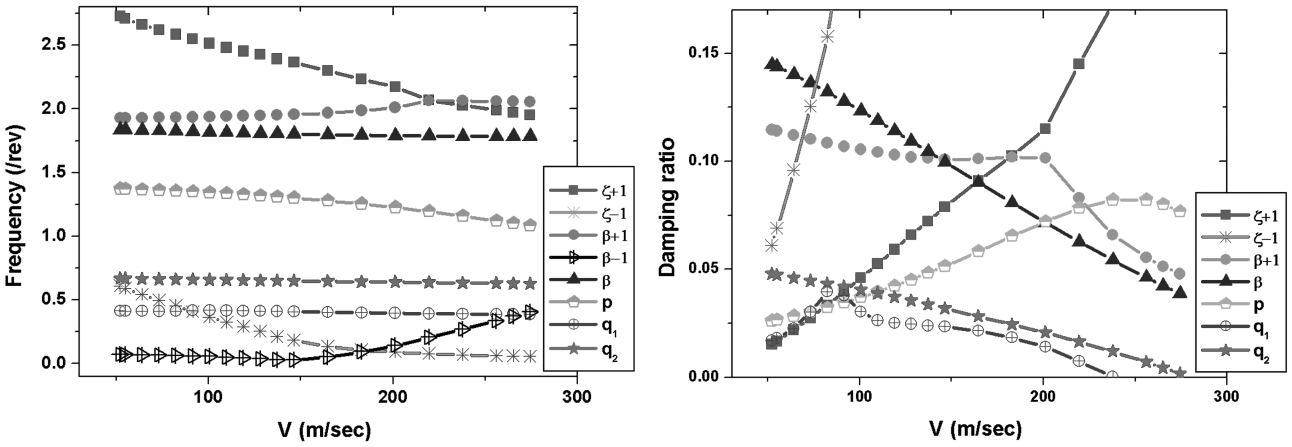

a) Frequency result b) Damping result

Fig. 4 Frequency and damping results in terms of the flight speed in the normal quasi-steady aerodynamic model.

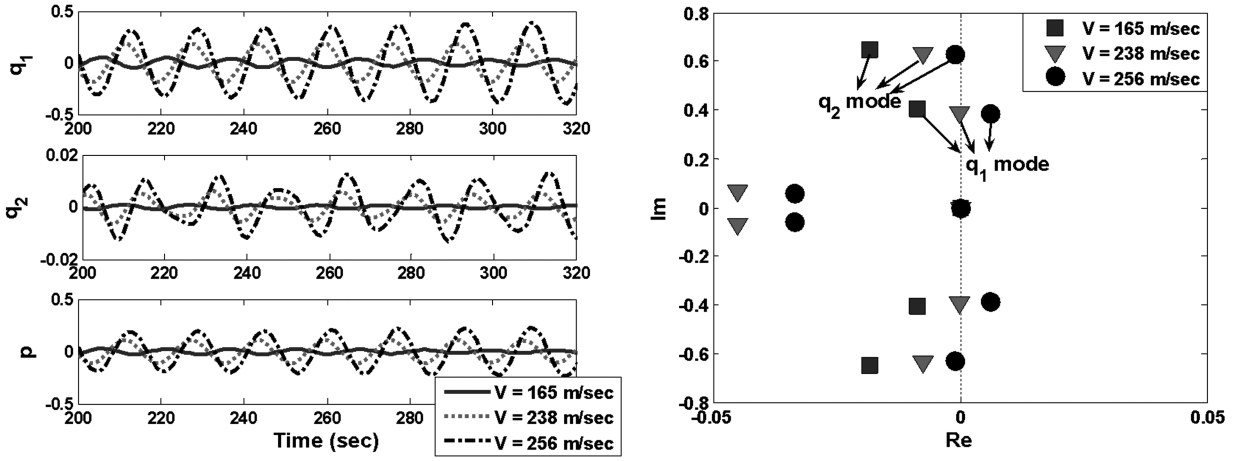

a) Time-domain result b) Frequency-domain result

Fig. 5 Time- and frequency-domain results using the normal quasi-steady aerodynamics.

B. Greenberg's Quasi-Steady Aerodynamic Model

The second aerodynamic model has a similar formulation with that for the normal quasi-steady aerodynamics. However, the lift formulation has a few different terms. According to Eq. (4), the first-order time-derivative terms $\dot{h}$ and $\dot{\theta}_{\text{ref}}$ are newly included in Greenberg's quasi-steady aerodynamic formulation. Here, $\dot{h}$ is velocity of the flapping motion, which is due to $-\delta u_P$ and δu_T components, and $\dot{\theta}_{\text{ref}}$ is an angular velocity of the pitch motion with respect to the inertial frame. They are presented in Appendix A.

In Fig. 6, the results of the frequency and damping for each mode show similar trends with those based on the previous normal quasi-steady aerodynamic model. However, the critical flight speed is slightly increased. Figure 6b clearly shows that q_1 mode becomes unstable at approximately $V = 240$ m/s among the modes. The precise flutter boundary may be extracted by the system pole result obtained from the eigenvalue analysis.

Figure 7 shows the result of the system poles, which represents the whirl-flutter stability boundary using Greenberg's present quasi-steady aerodynamics. According to the frequency-domain analysis, the flutter boundary is $V = 245$ m/s. When the flight speed becomes 245 m/s, the poles corresponding to the wing vertical bending mode q_1 are located on an imaginary axis. There is a slight discrepancy regarding the flutter boundary between the normal and Greenberg's aerodynamic models. Under Greenberg's present quasi-steady aerodynamics, flutter occurs at a slightly higher flight speed than it does under the normal quasi-steady aerodynamics.

C. Full Unsteady Aerodynamic Model

The quasi-steady aerodynamic model is believed to be incapable of describing a detailed aerodynamic environment in a tiltrotor aircraft. In this section, numerical investigation is conducted using the full unsteady aerodynamics.

In Fig. 8, the results of the frequency and damping for each mode show similar trends with those based on the previous quasi-steady aerodynamic models. However, the blade flapping modes exhibit a different behavior. The low-frequency mode of the blade flapping motion, $\beta - 1$, is not coincident with the wing modes until $V = 274$ m/s. The high-frequency mode of blade flapping motion, $\beta + 1$, does not coincide with the high-frequency blade lag mode, either. Because of this different behavior, it is observed that the low-frequency blade flapping mode increases the damping of the wing modes. The unsteady aerodynamic environment influences the blade flapping motion so that the estimated flutter speed may result in an increased value, which is due to the increase in the wing damping.

Figure 9 illustrates the frequency result while increasing the flight speed from 238 to 274 m/s. According to this result, the stability boundary is shown to be 265 m/s, based on the full unsteady aerodynamics.

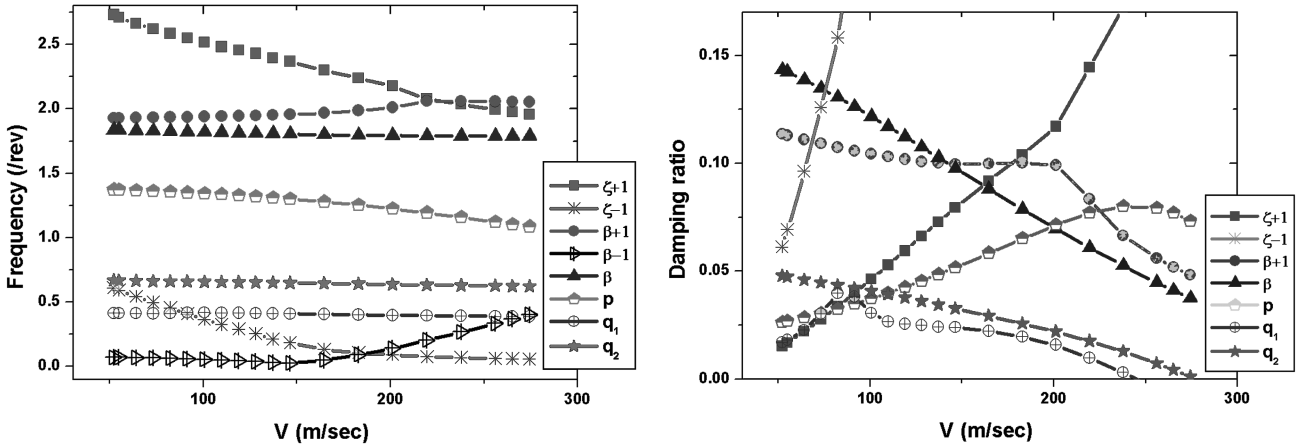

a) Frequency result b) Damping result

Fig. 6 Frequency and damping results in terms of the flight speed in Greenberg's quasi-steady aerodynamic model.

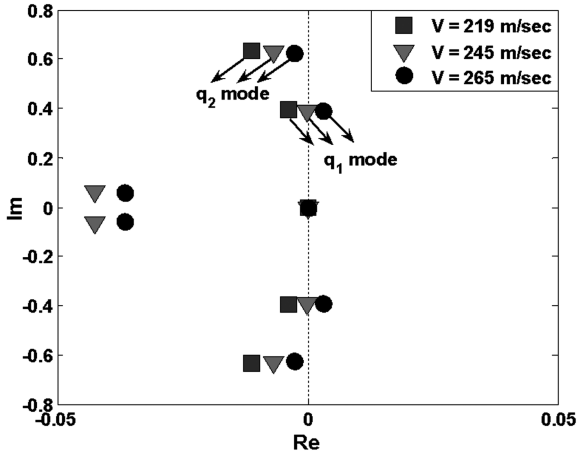

Fig. 7 Frequency-domain results using Greenberg's quasi-steady aerodynamics.

The critical flight speed is predicted to be the highest under the full unsteady aerodynamics when compared with those based on the quasi-steady aerodynamic models.

D. Comparison of the Results Among Three Aerodynamic Models Used

Figure 10 shows the comparison of the whirl-flutter stability in damping among the three aerodynamic models used. This result shows that the whirl-flutter stability is estimated to be the most conservative by the normal quasi-steady aerodynamic model, up to approximately 11%. Between the normal and Greenberg's quasi-steady aerodynamic models, the stability boundary based on Greenberg's model is overestimated by approximately 3%. It is clear that the full unsteady aerodynamic model provides the highest flutter speed. The background for such estimation is given in the previous section.

One of the reasons that the present analysis shows the varying flutter stability result is the different amount of aerodynamic damping introduced in the respective aerodynamics. The full unsteady aerodynamics assumes more aerodynamic damping than does the quasi-steady aerodynamics. A similar situation in a general fixed-wing aeroelastic problem is described well in [14]. It is observed that the flutter stability boundary is overestimated by the full unsteady aerodynamics due to such an assumption.

E. Validation with the Previous Predictions and Experiments

The present analysis is validated against the other existing numerical predictions provided in [2,18]. The comparison is illustrated in Fig. 11. Figure 11a shows the wing vertical bending q_1 compared with the other results based on a rigid blade without considering control system flexibility. The predicted trends for damping of the wing modes show good agreement. The model parameters used in the present analysis are the same as those used in [2]. Figure 11b shows the comparison with the experimental data, which are based on an experimental model with control system flexibility. There is a difference between the present result and the sophisticated elastic-blade models. The present model overestimates

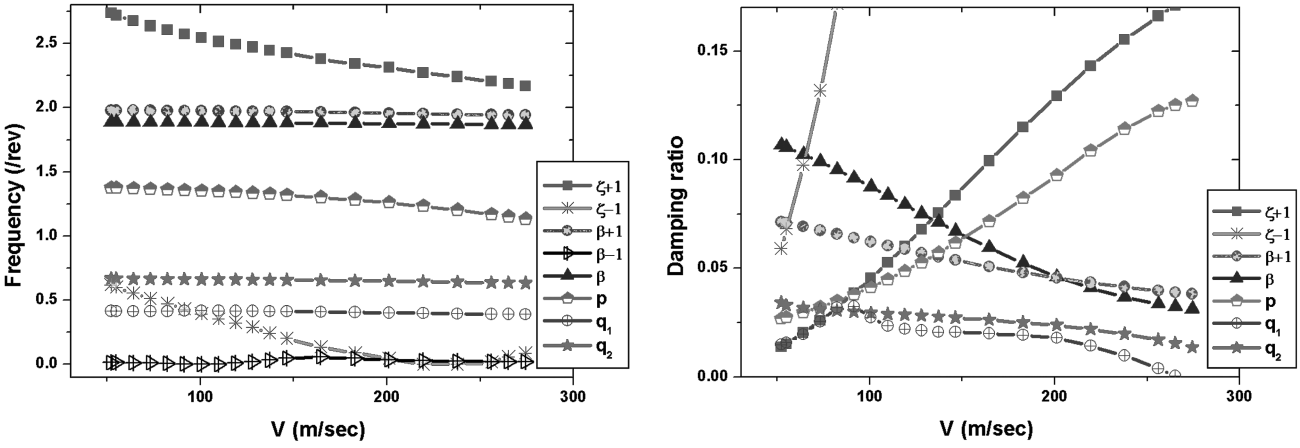

a) Frequency result b) Damping result

Fig. 8 Frequency and damping results in terms of the flight speed in full unsteady aerodynamic model.

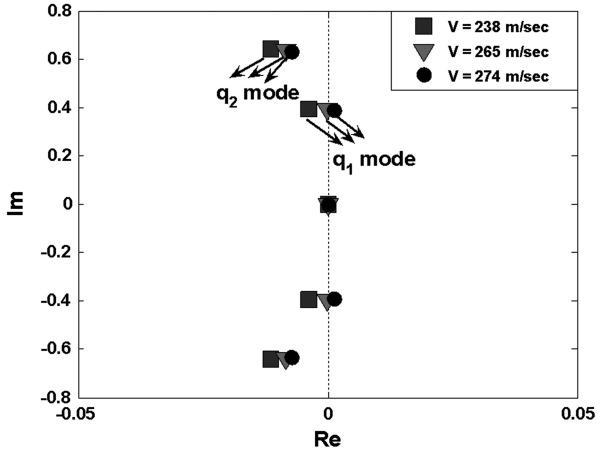

Fig. 9 Frequency-domain results using the full unsteady aerodynamics.

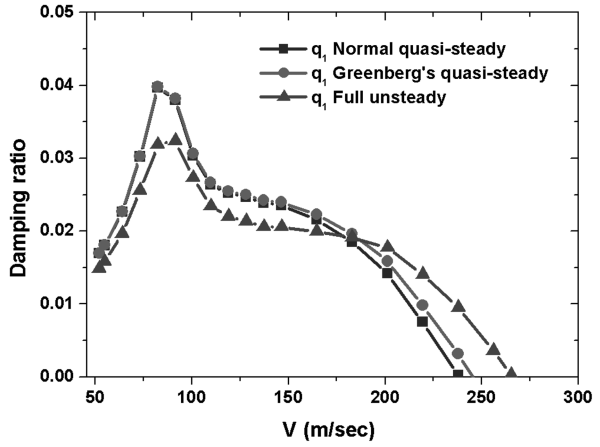

Fig. 10 Damping results of the wing vertical bending mode by each aerodynamic model.

the whirl-flutter speed against the sophisticated models by approximately 80 m/s. The blade elastic torsion motion and the control system flexibility are now regarded to be important factors for a precise stability boundary, because those factors were taken into account in the previous predictions.

F. Model Improvement Including the Control System Flexibility

Introducing a significant discrepancy regarding the stability boundary between the present analysis and the other existing results described in the previous section is the fact that the full-scale XV-15 aircraft and the previous models possess a flexible control system. However, the present model assumes a rigid control system. Hence, to obtain a capability for a more accurate stability-boundary prediction, a flexible control system needs to be modeled and included in the present model. In [4], a relationship between the control system flexibility and the kinematic couplings of the rotor system, such as pitch flap δ_3 and pitch lag δ_4, is presented. A detailed relationship between the control system stiffness and effective pitch-lag coupling can be expressed as follows:

$$K_{P\varsigma} = \frac{M_\beta}{I_P \omega_\theta^2} \tag{33}$$

In Eq. (33), it is apparent that the control system stiffness is inversely proportional to the pitch-lag coupling. If the control system is completely rigid, δ_4 will be zero. On the contrary, if it is considerably flexible, δ_4 will become infinite. Therefore, it is quite important to determine the correct degree of the flexibility in the control system. Figure 12 illustrates the variation of the pitch-flap and pitch-lag coupling parameters, measured from both XV-15 full-scale flight test [2] and the semispan model [18] in terms of the flight speed.

In the present model development, the control system is assumed to be completely rigid so that δ_4 may not be influenced, due to the fact that its numerical value is quite small compared with that of δ_3 under the perturbed blade pitch motion. However, if the control system is flexible, the perturbed blade pitch motion needs to be reformulated as follows:

$$\delta\theta = -\beta K_P - \varsigma K_{P\varsigma} \tag{34}$$

By substituting Eq. (34) into Eq. (11), an improved aeroelastic stability analysis is established and an updated analysis is conducted using the normal quasi-steady aerodynamics. Figure 13 shows the comparison results for the damping in the wing vertical bending q_1 between the presently improved analysis and the other existing numerical results. The predicted trend for the damping of the wing mode now shows better agreement.

G. Comparison of the Results Between the 9-DOF and 4-DOF Models

The present 9-DOF model is also compared with the 4-DOF model developed previously by the authors. The 4-DOF model takes into

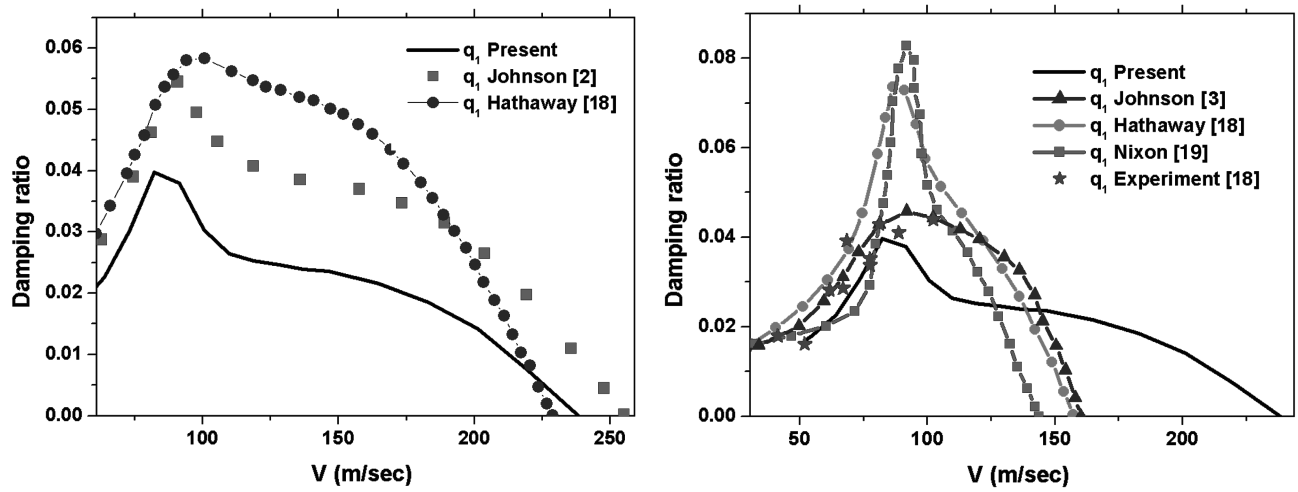

Fig. 11 Damping of the wing vertical bending mode in terms of the flight speed: a) rigid-blade model without control system flexibility and b) elastic-blade model with flexible control system and experimental data.

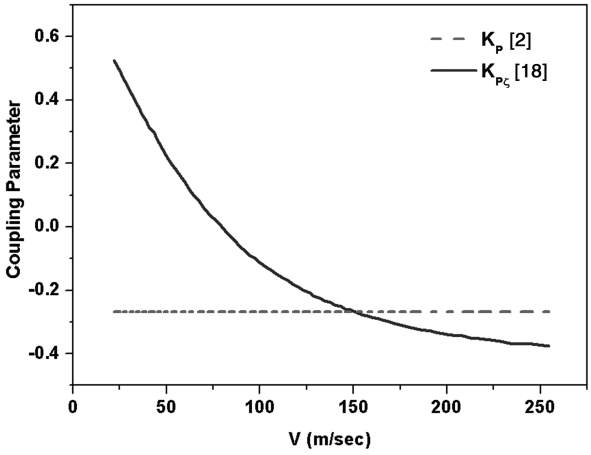

Fig. 12 Rotor coupling parameters measured in terms of the flight speed.

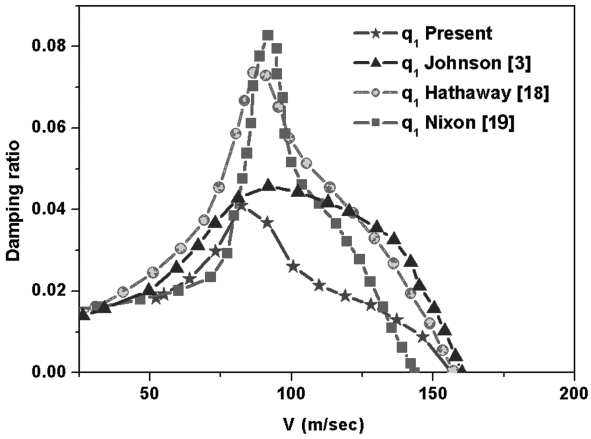

Fig. 13 Damping of the wing vertical bending mode, when including the flexible control system.

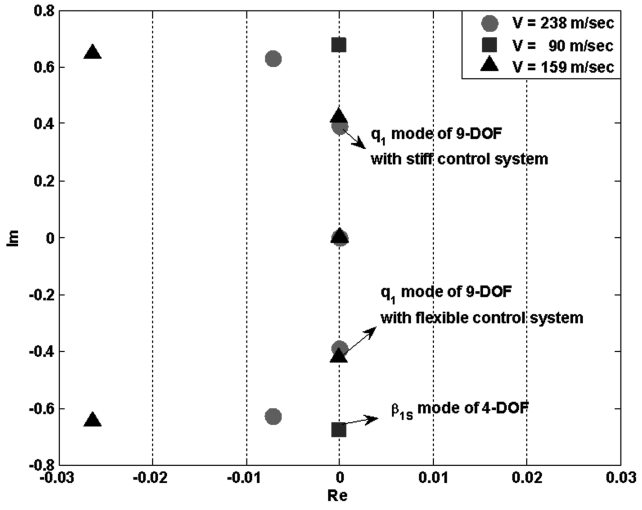

Fig. 14 Comparison of the flutter boundary between the 4-DOF and 9-DOF model under the normal quasi-steady aerodynamics.

account the blade flapping motion and rigid pylon motion only. The analytical procedures and results for the 4-DOF model are presented in [8]. Figure 14 shows the system pole results obtained from the 9-DOF model with both the completely rigid and flexible control systems, respectively, and from the 4-DOF model under the normal quasi-steady aerodynamics. In Fig. 14, it is observed that the instability is predicted to occur at $V = 238$, 90, and 159 m/s by the 9-DOF rigid, 4-DOF, and 9-DOF flexible models, respectively. It indicates that the present 9-DOF model with the flexible control system predicts the best-correlated flutter stability boundary compared with the other two models under the same aerodynamics, when those are compared with the result based on the sophisticated elastic-blade models. The present difference between the 9- and 4-DOF models is due to the inclusion of the wing, which is then connected with the rotor. The interaction between the wing and rotor creates the whirl-flutter phenomenon, and therefore the wing should be considered to estimate a precise whirl-flutter stability. However, the 4-DOF model does not include the wing degrees of freedom, and thus the β_{1S} mode of the rotor system exhibits instability instead.

Figure 14 also illustrates an influence of the control system flexibility on the whirl-flutter stability boundary. If the control system becomes stiffer, the flutter stability boundary is increased significantly, because the control system flexibility generally influences the kinematic couplings and varies the flutter stability boundary of the aircraft, as described in the previous section [4,18].

V. Conclusions

Time- and frequency-domain analyses are conducted using a newly developed analysis for whirl-flutter stability in tiltrotor aircraft with a rigid blade and elastic wing. The frequency and damping of each mode are also calculated. Two quasi-steady and an unsteady aerodynamic models are used to predict the whirl-flutter stability boundary. The developed model shows good agreement with the other existing numerical analyses. Investigations of the influence with respect to different aerodynamic models are concluded as follows:

1) The flutter speeds based on the two quasi-steady aerodynamic models are close to each other. However, the full unsteady aerodynamic model predicts that the whirl-flutter instability occurs at a higher speed than that predicted by the quasi-steady aerodynamic models. Also, it is found that the critical mode of flutter is related with the elastic-wing modes.

2) The low frequencies of the blade flap and lag motion, which are $\beta - 1$ and $\varsigma - 1$, are found to be quite related with the aircraft stability. The low frequency of the blade lag motion influences stability under the quasi-steady aerodynamic model. However, the low frequency of the blade flapping motion influences stability under the unsteady aerodynamic model. According to the preceding results, the major components that affect the aircraft stability are the regressive modes of the rotor.

3) The present model is validated against other existing numerical and experimental data. Because the wing vertical bending mode becomes unstable first, the vertical bending mode is compared as a function of the flight speed. The estimated trends of damping mode are in good agreement. The present results and the existing data show a similar flutter stability boundary.

4) The control system flexibility is considered in the present model with a relationship between control system stiffness and effective pitch-lag coupling. The proper pitch-lag coupling value is selected in terms of flight speed. The flutter analysis is accomplished with normal quasi-steady aerodynamics. The wing vertical bending mode is compared with the present model and other existing models. The predictions of damping mode show good correlation each other. Whole models have a similar flutter stability boundary: approximately 150 m/s.

5) The flutter stability boundary predicted by the present 9-DOF model including the flexible control system gives better correlation than that by the previous 4-DOF model under the same aerodynamic models. By comparing the results between the stiff and flexible control systems using the 9-DOF model, a stiffer control system gives an increased flutter boundary.

Appendix A: Perturbation Velocity Expression

The perturbation terms of the velocity are presented in Eqs. (A1–A3). Equation (A4) presents the trim and perturbation expressions in

the blade pitch term. Equations (A5) and (A6) are used in Greenberg's quasi-steady and unsteady aerodynamic models. In Eq. (A5), $K_P = \tan\delta_3$.

$$\begin{aligned}\delta\bar{u}_T &= \bar{r}(\dot{\alpha}_Z - \dot{\varsigma}) - \bar{h}(\dot{\alpha}_y \sin\psi_m + \dot{\alpha}_x \cos\psi_m)\\ &\quad + (\bar{V} + \bar{v})(\alpha_y \sin\psi_m + \alpha_x \cos\psi_m)\\ &\quad + \bar{V}(\beta_G \cos\psi_m + \alpha_G \sin\psi_m) + (\dot{y}_P \cos\psi_m - \dot{x}_P \sin\psi_m)\\ &= \bar{r}\delta\bar{u}_{T_A} + \delta\bar{u}_{T_B}\end{aligned} \tag{A1}$$

$$\begin{aligned}\delta\bar{u}_P &= \bar{r}(\dot{\beta} - \dot{\alpha}_y \cos\psi_m + \dot{\alpha}_x \sin\psi_m) + (\bar{V}u_G + \dot{z}_P)\\ &= \bar{r}\delta\bar{u}_{P_B} + \delta\bar{u}_{P_A}\end{aligned} \tag{A2}$$

$$\delta U = \frac{u_{T_0}}{U_0}\delta u_T + \frac{u_{p_0}}{U_0}\delta u_p, \qquad \delta\dot{U} = \frac{u_{T_0}}{U_0}\delta\dot{u}_T + \frac{u_{p_0}}{U_0}\delta\dot{u}_p \tag{A3}$$

$$\theta_0 = \alpha_0 + \phi_0 = \alpha_0 + \tan^{-1}\frac{u_{P_0}}{u_{T_0}} \simeq \alpha_0 + \frac{u_{P_0}}{u_{T_0}} \tag{A4}$$

$$\delta\theta_{\text{ref}} = -K_p\beta + \alpha_y \cos\psi - \alpha_x \sin\psi \tag{A5}$$

$$\dot{h} = -\delta u_p \cos\phi + \delta u_T \sin\phi \tag{A6}$$

Appendix B: Governing Equation

The governing equation with quasi-steady aerodynamic models is presented in a matrix form as follows:

$$\underbrace{A\ddot{x} + B\dot{x} + Cx}_{\text{structural part}} = \underbrace{D}_{\text{aerodynamic part}} \tag{B1}$$

where the relevant matrices are as follows:

$$A = \begin{bmatrix}
I^*_\beta & 0 & 0 & 0 & 0 & 0 & 0 & 0 & -I^*_{\beta_\alpha} \\
0 & I^*_\beta & 0 & 0 & 0 & 0 & 0 & -I^*_{\beta_\alpha}\bar{\eta}'_w & 0 \\
0 & 0 & I^*_\varsigma & 0 & 0 & 0 & 0 & -\bar{\eta}'_w h_m S^*_\varsigma & 0 \\
0 & 0 & 0 & I^*_\varsigma & 0 & 0 & S^*_\varsigma \bar{y}_{T_w} & 0 & S^*_\varsigma h_m \\
0 & 0 & 0 & 0 & I^*_{\beta_0} & 0 & 0 & -S^*_{\beta_0}\bar{y}_{T_w} & 0 \\
0 & 0 & 0 & 0 & 0 & I^*_{\varsigma_0} & I^*_{\varsigma_0\alpha}\bar{\eta}'_w & 0 & 0 \\
0 & 0 & 0 & S^*_\varsigma \bar{y}_{T_w} & 0 & 0 & (I^*_{q_w} + m^*_p) + \bar{y}^2_{T_w}2M_b & 0 & S^*_w + 2h_m\bar{y}_{T_w}M_b \\
0 & 0 & -S^*_\varsigma h_m\bar{\eta}'_w & 0 & -2\bar{y}_{T_w}S^*_{\beta_0} & 0 & 0 & (I^*_{q_w} + I^*_{p_x}\bar{\eta}'^2_w + m^*_p) & +h^2_m\bar{\eta}'^2_w 2M_b + \bar{y}^2_{T_w}2M_b \quad 0 \\
0 & 0 & 0 & S^*_\varsigma h_m & 0 & 0 & S^*_w + 2h_m\bar{y}_{T_w}M_b & 0 & (I^*_{q_w} + I^*_{p_y}) + 2h^2_m M_b
\end{bmatrix} \tag{B2}$$

$$B = \begin{bmatrix}
0 & 2I^*_\beta & 0 & 0 & 0 & 0 & 0 & -2I^*_{\beta_\alpha}\bar{\eta}'_w & 0 \\
-2I^*_\beta & 0 & 0 & 0 & 0 & 0 & 0 & 0 & 2I^*_{\beta_\alpha} \\
0 & 0 & 0 & 2I^*_\varsigma & 0 & 0 & 0 & 0 & 0 \\
0 & 0 & -2I^*_\varsigma & 0 & 0 & 0 & 0 & 0 & 0 \\
0 & 0 & 0 & 0 & 0 & 0 & 0 & 0 & 0 \\
0 & 0 & 0 & 0 & 0 & 0 & 0 & 0 & 0 \\
0 & 0 & 0 & 0 & 0 & 0 & C^*_{q_1} & 0 & 0 \\
0 & 0 & 0 & 0 & 0 & 0 & 0 & C^*_{q_2} & 0 \\
0 & 0 & 0 & 0 & 0 & 0 & 0 & 0 & C^*_p
\end{bmatrix} \tag{B3}$$

$$C = \begin{bmatrix}
I^*_\beta(\bar{\nu}^2_\beta - 1) & 0 & 0 & 0 & 0 & 0 & 0 & 0 & 0 \\
0 & I^*_\beta(\bar{\nu}^2_\beta - 1) & 0 & 0 & 0 & 0 & 0 & 0 & 0 \\
0 & 0 & I^*_\varsigma(\bar{\nu}^2_\zeta - 1) & 0 & 0 & 0 & 0 & 0 & 0 \\
0 & 0 & 0 & I^*_\varsigma(\bar{\nu}^2_\zeta - 1) & 0 & 0 & 0 & 0 & 0 \\
0 & 0 & 0 & 0 & I^*_{\beta_0}\bar{\nu}^2_{\beta_0} & 0 & 0 & 0 & 0 \\
0 & 0 & 0 & 0 & 0 & I^*_{\zeta_0}\bar{\nu}^2_{\zeta_0} & 0 & 0 & 0 \\
0 & 0 & 0 & 0 & 0 & 0 & K^*_{q_q} & 0 & 0 \\
0 & 0 & 0 & 0 & 0 & 0 & 0 & K^*_{q_2} & 0 \\
0 & 0 & 0 & 0 & 0 & 0 & 0 & 0 & K^*_p
\end{bmatrix} \tag{B4}$$

$$\begin{aligned}D^T &= \left\{\left(\gamma\frac{\bar{M}_{F_{1c}}}{a\bar{c}}\right)_{\text{rotor}}, \left(\gamma\frac{\bar{M}_{F_{1s}}}{a\bar{c}}\right)_{\text{rotor}}, \left(\gamma\frac{\bar{M}_{L_{1c}}}{a\bar{c}}\right)_{\text{rotor}}, \left(\gamma\frac{\bar{M}_{L_{1s}}}{a\bar{c}}\right)_{\text{rotor}}, \left(\gamma\frac{\bar{M}_{F_0}}{a\bar{c}}\right)_{\text{rotor}}, \left(\gamma\frac{\bar{M}_{L_0}}{a\bar{c}}\right)_{\text{rotor}}, \gamma\frac{2(\bar{M}_{q_1})_{\text{aero}}}{\sigma a}\right.\\ &\quad + \left(\gamma 2\bar{\eta}'_w\frac{C_Q}{\sigma a} + \gamma\bar{y}_{T_w}\frac{2C_H}{\sigma a}\right)_{\text{rotor}}, \gamma\frac{2(\bar{M}_{q_2})_{\text{aero}}}{\sigma a} + \left(-\gamma\bar{\eta}'_w\frac{2C_{M_x}}{\sigma a} + \gamma\bar{\eta}'_w\bar{h}\frac{2C_y}{\sigma a} - 2\gamma\bar{y}_{T_w}\frac{C_T}{\sigma a}\right)_{\text{rotor}}, \gamma\frac{2(\bar{M}_p)_{\text{aero}}}{\sigma a}\\ &\quad \left. + \left(\gamma\frac{2C_{M_y}}{\sigma a} + \gamma\bar{h}\frac{2C_H}{\sigma a} - \gamma 2C^*_{pq}\bar{y}_{T_w}q_1\frac{C_T}{\sigma a}\right)_{\text{rotor}}\right\}\end{aligned} \tag{B5}$$

Acknowledgments

This research was supported by Korea Aerospace Research Institute under the Korean Helicopter Project Dual-Use Component Development Program funded by the Ministry of Commerce, Industry, and Energy and also partially by grant no. R01-2005-000-10059-0 from the Basic Research Program of the Korea Science and Engineering Foundation.

References

[1] Hall, W. E., Jr., "Prop-Rotor Stability at High Advance Ratios," *Journal of the American Helicopter Society*, Vol. 11, No. 2, Apr. 1966, pp. 11–26.

[2] Johnson, W., "Dynamics of Tilting Proprotor Aircraft in Cruise Flight," NASA, TN D-7677, May 1974.

[3] Johnson, W., "Analytical Modeling for Tilting Proprotor Aircraft Dynamics Including Blade Torsion and Coupled Bending modes, and Conversion Mode Operation," NASA TM X-62, 369, Aug. 1974.

[4] Johnson, W., "Analytical Modeling Requirements for Tilting Proprotor Aircraft Dynamics," NASA TN D-8013, July 1975.

[5] Nixon, M. W., Kvaternik, R. G., and Settle, T. B., "Tiltrot Vibration Reduction Through Higher Harmonic Control," *American Helicopter Society 53rd Annual Forum* [CD-ROM], AHS International, Alexandria, VA, 29 Apr.–1 May 1997.

[6] Kvaternik, R. G., Piatak, D. J., Nixon, M. W., Langston, C. W., Singleton, J. D., Bennett, R. L., and Brown, R. K., "An Experimental Evaluation of Generalized Predictive Control for Tiltrotor Aeroelastic Stability Augmentation in Airplane Mode of Flight," *American Helicopter Society 57th Annual Forum* [CD-ROM], AHS International, Alexandria, VA, 9–11 May 2001.

[7] Singh, R., and Gandhi, F., "Wing Flaperon and Swashplate Control for Whirl Flutter Stability Augmentation of a Soft In-Plane Tiltrotor," *31st European Rotorcraft Forum* [CD-ROM], Royal Aeronautical Society, London, 13–15 Sept. 2005.

[8] Kim, T., Shin, S. J., and Kim, T., "Time and Frequency Domain Analysis of Whirl Flutter Stability in Tiltrotor Aircraft," *47th AIAA/ASME/ASCE/AHS/ASC Structures, Structural Dynamics, and Materials Conference* [CD-ROM], AIAA, Reston, VA, May 2006.

[9] Bisplinghoff, R. L., Ashley, H., and Halfman, R. L., *Aeroelasticity*, Dover, New York, 1996, Chap. 6.

[10] Greenberg, J. M., "Airfoil in Sinusoidal Motion in Pulsating Stream," NASA TN 1326, 1947.

[11] Dinyavari, M. A. H., and Friedmann, P. P., "Unsteady Aerodynamics in Time and Frequency Domains for Finite Time Arbitrary Motion of Rotary Wings in Hover and Forward Flight," *25th AIAA/ASME/ASCE/AHS Structures, Structural Dynamics, and Materials Conference*, AIAA, New York, May 1984, pp. 226–282.

[12] Friedmann, P. P., and Yuan, C., "Effect of Modified Aerodynamic Strip Theories on Rotor Blade Aeroelastic Stability," *AIAA Journal*, Vol. 15, No. 7, July 1977, pp. 932–940.

[13] Dinyavari, M. A. H., and Friedmann, P. P., "Application of Time-Domain Unsteady Aerodynamics to Rotary-Wing Aeroelasticity," *AIAA Journal*, Vol. 24, No. 9, Sept. 1986, pp. 1423–1432.

[14] Cesnik, C. E. S., *16.242 Aeroelasticity*, Dept. of Aeronautics and Astronautics, Massachusetts Inst. of Technology, Cambridge, MA, Feb. 1998.

[15] Friedmann, P. P., and Robinson, L. H., "Influence of Unsteady Aerodynamics on Rotor Blade Aeroelastic Stability and Response," *AIAA Journal*, Vol. 28, No. 10, Dec. 1990, pp. 1806–1812.

[16] Jones, R. T., "The Unsteady Lift of a Wing of Finite Aspect Ratio," NACA, Rept. 681, 1940.

[17] Jones, R. T., "Operational Treatment of the Nonuniform Lift Theory to Airplane Dynamics," NACA TN 667, 1938.

[18] Hathaway, E. L., "Active and Passive Techniques for Tiltrotor Aeroelastic Stability Augmentation," Ph.D. Thesis, Graduate School College of Engineering, Pennsylvania State Univ., State College, PA, Aug. 2005.

[19] Nixon, M. W., "Aeroelastic Response and Stability of Tiltrotors with Elastically-Coupled Composite Rotor Blades," Ph.D. Thesis, Univ. of Maryland, College, Park, MD, 1993.